Journal of
Materials Chemistry A

PAPER

View Article Online
View Journal | View Issue

Cite this: *J. Mater. Chem. A*, 2019, **7**, 11836

"Hot edges" in an inverse opal structure enable efficient CO_2 electrochemical reduction and sensitive *in situ* Raman characterization†

Yang Yang,[ab] Lukas Ohnoutek,[cd] Saira Ajmal,[a] Xiuzhen Zheng,[a] Yiqing Feng,[a] Kejian Li,[a] Tao Wang,[a] Yue Deng,[a] Yangyang Liu,[a] Dong Xu,[a] Ventsislav K. Valev*[cd] and Liwu Zhang*[ab]

Received 1st March 2019
Accepted 9th April 2019

DOI: 10.1039/c9ta02288k

rsc.li/materials-a

Conversion of CO_2 into fuels and chemicals *via* electroreduction has attracted significant interest. *Via* mesostructure design to tune the electric field distribution in the electrode, it is demonstrated that the Cu–In alloy with an inverse opal (CI-1-IO) structure provides efficient electrochemical CO_2 reduction and allows for sensitive detection of the CO_2 reduction intermediates *via* surface-enhanced Raman scattering. The significant enhancement of Raman signals of the intermediates on the CI-1-IO surface can be attributed to electric field enhancement on the "hot edges" of the inverse opal structure. Additionally, a highest CO_2 reduction faradaic efficiency (FE) of 92% (sum of formate and CO) is achieved at −0.6 V *vs.* RHE on the CI-1-IO electrode. The diffuse reflectance infrared Fourier transform spectroscopy (DRIFTS) results show that the Cu–In alloy with an inverse opal structure has faster adsorption kinetics and higher adsorption capacity for CO_2. The "hot edges" of the bowl-like structure concentrate electric fields, due to the high curvature, and also concentrate K^+ on the active sites, which can lower the energy barrier of the CO_2 reduction reaction. This research provides new insight into the design of materials for efficient CO_2 conversion and the detection of intermediates during the CO_2 reduction process.

1. Introduction

Electrochemical reduction of carbon dioxide (CO_2) is a promising way to convert CO_2 to carbon-based fuels and chemicals using renewable electricity.[1–5] However, its application often suffers from low conversion efficiency, poor selectivity and lesser-known intermediates.[3,6] Consequently, substantial efforts have been devoted to designing electrodes with efficient CO_2 reduction activity, such as controlling the size and morphology, tuning electrolytes, introducing metal-oxide interfaces, fabricating porous structures *etc.*[1,7–13] By coupling another metal species to form an alloy might reconstruct the catalyst interface, which could change the binding energy of intermediates on the surface during the CO_2 reduction reaction resulting in controllable selectivity.[14–21] Yet another method to facilitate CO_2 reduction efficiency and selectivity consists of introducing an inverse opal structure.[22,23] Surendranath's group has designed Au and Ag inverse opal thin films with different thicknesses, which show a significant diminution of the hydrogen evolution reaction (HER) with increasing porous thin film thickness.[22,23] A Cu inverse opal structure derived from Cu_2O inverse opal was reported to show improved catalytic activity and selectivity for the CO_2 electrochemical reduction due to the porous structure.[24] However, previous work on inverse opal mainly focused on the effects of diffusional gradients within the pores, while many of the specific properties of inverse opal structures remain unexplored; such important properties include photonic Bragg resonances, electric field concentrations on the edges of the mesostructure and their potential effects on CO_2 reduction and *in situ* measurements.

In situ measurements have been playing an increasingly important role in the study of the CO_2 reduction mechanism. Such measurements include *in situ* Raman spectroscopy, *in situ* attenuated total reflectance-Fourier transform infrared spectroscopy (ATR-FTIR), vibrational sum-frequency generation spectroscopy (VSFG), operando extended X-ray absorption fine structure (EXAFS) *etc.*[14,16,25–30] Among these measurements, *in situ* Raman spectroscopy is an efficient and simple method for detecting the intermediates during CO_2 reduction.[31–39] However, the Raman signals of the intermediates are very weak, which

---

[a] *Shanghai Key Laboratory of Atmospheric Particle Pollution and Prevention, Department of Environmental Science and Engineering, Fudan University, Shanghai, 200433, P. R. China. E-mail: zhanglw@fudan.edu.cn*

[b] *Shanghai Institute of Pollution Control and Ecological Security, Shanghai, 200092, Peoples' Republic of China*

[c] *Centre for Photonics and Photonic Materials, University of Bath, Bath, BA2 7AY, UK. E-mail: v.k.valev@bath.ac.uk*

[d] *Centre for Nanoscience and Nanotechnology, University of Bath, Bath, BA2 7AY, UK*

† Electronic supplementary information (ESI) available. See DOI: 10.1039/c9ta02288k

makes the signals hard to detect.[16,27] Generally, a typical electrochemical Raman cell contains electrodes, an electrolyte layer and a quartz window. The low sensitivity of Raman spectroscopy can be attributed to the limited optical path and mismatch of the refractive indices of media.[40] Using an immersion objective with a long working distance reduces the loss of Raman signals and improves the detection sensitivity, spatial resolution, and electrochemical response.[23,40,41] However, this approach is usually expensive and complex. Nanostructure-based surface enhanced Raman spectroscopy (SERS) is also an effective method for surface analysis,[42] which achieves ultrahigh sensitivity down to the single molecule level by utilizing coinage-metal (such as Au, Ag and Cu) nanostructures.[42,43] Developing electrodes with both good SERS ability and catalytic activity for *in situ* investigation of the process of CO_2 reduction is still a challenge.

Herein, by depositing a monolayer of an inverse opal structured Cu–In alloy, we present a system rich in "hot edges" for CO_2 reduction and *in situ* Raman investigation. The Raman signals are dramatically enhanced compared to the case when a Cu–In alloy without an inverse opal structure is used. Furthermore, the current density, FE_{HCOO^-} and FE_{CO} are also significantly improved by introducing the inverse opal structure. The DRIFTS results demonstrate that CI-1-IO with an inverse opal structure exhibits faster adsorption kinetics and higher capacity for CO_2 adsorption, which might benefit the CO_2 conversion. The greatly enhanced Raman signal is attributed to local field enhancements, demonstrated by finite-difference time-domain (FDTD) simulations. This Raman signal then enables the *in situ* study of the CO_2 reduction process. The high-curvature structure concentrates electric fields, thus K^+ ions gather on the active sites ("hot edges"). Density functional theory (DFT) calculations further demonstrate that the adsorbed K^+ ions lower the energy barrier of the CO_2 reduction reaction (CO_2RR), which facilitates CO_2 conversion.

2. Experimental

2.1 Chemicals

Styrene (Aldrich, 99%) and $K_2S_2O_8$ (AR, Sinopharm Chemical Reagent Co., China) were used to prepare polystyrene (PS) opal templates. Formic acid and acetic acid standard samples (Sigma), $NaHCO_3$ and $NaCO_3$ (Sigma, 99%) were used for ion chromatograph (IC). The other reagents were purchased from Sinopharm Chemical Reagent Co., China. Fluoride-tin oxide (FTO) glasses (thickness, 1 mm) were purchased from China Southern Glass Co. Ltd. All chemical reagents were of analytical grade and used without any further purification. Deionized (DI) water was used throughout the experiment. The FTO glasses were sonicated while being immersed in piranha solution, ethanol and DI water in sequence to remove the impurities on the surface.

2.2 Preparation of polystyrene spheres

Monodisperse polystyrene spheres (PS) with a diameter of about 360 nm were synthesized according to the process reported in the literature.[44] Typically, 100 mL of ultrapure water (18 MΩ cm^{-2}) and 0.6 g of styrene (washed with 5% NaOH solution to remove the polymerization inhibitor) were added into a three-necked, round-bottomed flask (250 mL). The mixture was stirred at 500 rpm, while being heated to 70 °C and purged with nitrogen gas with a flow rate of 70 mL min^{-1}. Afterwards, the mixture was kept at 70 °C for 20 min, then 0.12 g of $K_2S_2O_8$ was added and the mixture was kept for 12 h. The oversized and undersized particles of the precursor solution of PS were removed by high-speed centrifugation. The first centrifugation was used to remove the undersized PS and the second one to remove the oversized PS microspheres. At the end of the process, the average particle diameter of the PS was approximately 360 nm.

The concentration of PS was diluted to 0.03% (mass fraction) using DI water. Subsequently, the FTO glass was immersed vertically into the PS colloid solution. Then, the solution with the glass was placed in a furnace and kept at 55 °C until the water entirely evaporated. The PS opal templates self-assembled on the FTO with a close-packed structure, named FTO-PS.

2.3 Preparation of the CuIn film with and without an inverse opal structure

The Cu–In alloy was prepared using an electrodeposition method reported by Yuan *et al.* with a minor modification.[45] First, 5 mmol of $CuCl_2 \cdot 2H_2O$, was added to a solution containing 0.2 mmol of triethanolamine and 0.015 mmol of sodium citrate. Then, 5 mmol of $InCl_3 \cdot 4H_2O$ was added to the solution. Finally, the pH of the solution was adjusted to 4 using H_2SO_4 and NaOH.

2.3.1 Preparation of the Cu–In film without an inverse opal structure. FTO conductive glass, a saturated calomel electrode and platinum foil were used as the working electrode, reference electrode and counter electrode, respectively. Electrodeposition was conducted at −1 V (*vs.* SCE) for 30 min at 30 °C. The sample was named CI-1.

2.3.2 CuIn film with an inverse opal structure (CI-1-IO). For the CI-1-IO preparation, FTO-PS was used as the working electrode and the other electrodeposition conditions were kept the same as for CI-1. After electrodeposition, the sample was dried in air flow, and then immersed into tetrahydrofuran (THF) solution for 30 min to remove the PS template. Later, the sample was washed with ethanol and water. We denote this sample as CI-1-IO. Scheme S1 (ESI†) illustrates the preparation procedure of the PS opal template and the CI-1-IO sample.

2.4 Characterization

X-ray diffraction (XRD) patterns were measured using a Bruker D8 Advance X-ray diffractometer with Cu Kα radiation. The accelerating voltage and applied current were 40 kV and 40 mA, respectively. The general morphology imaging and elemental mapping of the samples were conducted using a field emission scanning electron microscopy (FESEM, Sigma Zeiss 150, Cal Zeiss Co., Germany) instrument operated at 5 kV and using scanning transmission electron microscopy (STEM, Phenom ProX, at 15 kV) with energy-dispersive spectroscopy (EDS). The photoelectrochemical data were collected using an IVIUM electrochemical workstation. The *in situ* DRIFTS spectra were collected on a Shimadzu Tracer-100 FTIR spectrometer equipped with a high-sensitivity mercury cadmium telluride (MCT) detector cooled by liquid nitrogen. A temperature controller was coupled with the DRIFTS chamber (Praying Mantis Kit, Harrick). Samples were placed in a ceramic sample cup (0.35 mm depth, 5 mm i.d.). A series of spectra were recorded every 2 minutes with 100 scans averaged for each spectrum and a resolution of 4 cm^{-1}. The *in situ* Raman spectra were measured on an XploRA confocal spectrometer (Jobin Yvon, Horiba Gr, France) with a charge coupled device (CCD) detector. Raman scattering was excited using an external-cavity diode laser (785 nm, with 25% energy, ~25 mW) coupled with a 10× Olympus microscope objective. A holographic notch filter was used to filter out the excitation line and a holographic grating (1200 gr mm^{-1}) was employed for spectral mapping. A CCD with 1024 × 256 pixels was used to collect the spectra with a resolution of 1.2 cm^{-1}, with 2 accumulations at 2 s acquisition time.

2.5 Electrochemical reduction of CO_2

All electrochemical measurements were carried out on an IVIUM electrochemical workstation using a conventional three-electrode system. A platinum plate and an Ag/AgCl electrode was used as the counter and reference electrode, respectively. The anode and cathode compartment of the electrochemical cell were separated using a Nafion 117 membrane. Before the measurement, CO_2 was bubbled into 50 mL of 0.1 M $KHCO_3$ electrolyte solution for 30 minutes to reach saturation. The gaseous products were analyzed using a gas chromatograph (SHIMADZU, GC-2014) equipped with TDX-1 and HT-POLT Al_2O_3/S columns. A thermal conductivity detector (TCD) was mainly used to detect and quantify H_2, a flame ionization detector (FID) with a methanizer was used to analyze and quantify CO using the TDX-1 column, and another FID was used for separating and quantifying CH_4 and other alkane contents with the HT-POLT Al_2O_3/S column. Ar (99.999%) was used as the carrier gas. Liquid products were analyzed using ion chromatography (IC, Metrohm, 883 Basic IC Plus with Metrosp A SUPP 5-250 column) and ^1H nuclear magnetic resonance (NMR, AVANCE III HD, 500 MHz, Bruker) spectra. In order to confirm the organic products in solution, 0.5 mL of liquid produced was mixed with 0.1 mL of D_2O containing 0.01 μL of dimethyl sulfoxide (DMSO) as the internal standard for a one-dimensional ^1H NMR spectrum test. Typically, the peak at about 8.3 ppm corresponds to formic acid (HCOOH) and the peak at ∼2.6 ppm represents DMSO. To quantify the formate, the solution was diluted 10 times with ultrapure water, then injected into an IC instrument. Data are shown in the ESI (Fig. S14–S16†).

2.6 Density functional theory (DFT) calculations on the Cu_2In surface

DFT calculations were performed with the Vienna Ab initio Simulation Package (VASP) using the projector augmented wave (PAW) method with the exchange–correlation functional of Perdew–Burke–Ernzehof (PBE) and generalized gradient approximation (GGA).[3,46–48] The (001), (010), (100) and (110) slabs of Cu_2In were constructed using a 4 × 4 × 1 supercell and separated by 12 Å of vacuum. The PAW pseudopotentials were used to calculate the interaction between ions and electrons in a plane wave basis set with a cut-off energy of 500 eV and 4 × 4 × 1 *k*-points. The Gibbs free energies (ΔG) were calculated at 298.15 K and 1 atm, as outlined below:[49]

$$G = H - T\Delta S = E_{\text{DFT}} + E_{\text{ZPE}} + \int_0^{298.15} C_{\text{v}}\text{d}T - T\Delta S$$

where E_{DFT} is the optimized total energy, E_{ZPE} is the zero-point vibrational energy, $\int_0^{298.15} C_{\text{v}}\text{d}T$ is the heat capacity, H is the enthalpy, T is the temperature and ΔS is the entropy. The change in ΔG between reaction steps of the CO_2 to CO reaction coordinate was calculated from the computational hydrogen electrode model.[50] Moreover, the binding energy was calculated from DFT-optimized structures as follows: $E_{\text{binding}} = E_{\text{CO}_2^*} - (E_{\text{Cu}_2\text{In}} + E_{\text{CO}_2})$, where $E_{\text{CO}_2^*}$ is the energy of the system with CO_2 proximate to the Cu_2In surface, $E_{\text{Cu}_2\text{In}}$ is the energy of the Cu_2In surface (with and without K^+ for the respective cases) and E_{CO_2} is the energy of CO_2 gas.

2.7 FDTD and COMSOL simulations

For these simulations, the Lumerical Finite Difference Time Domain (FDTD) software was used to calculate the electric fields in the vicinity of the nanostructured surface of the sample CI-1-IO. Simulations were performed for a hexagonal arrangement of the bowl-like structures on the surface. Periodic boundary conditions were applied on the edges of the unit cell. It was assumed that the patterned layer consisted of the Cu_2In alloy. The permittivity spectra of the alloy were calculated using Bruggeman effective medium approximation. In the model, the structures were irradiated with a linearly polarized broadband optical pulse and the electric field on the surface and in the longitudinal section was monitored.

Simulations of the free electron density on the working electrode with an inverse opal structure were performed with the COMSOL Electric Currents module. The simulated system consisted of two electrodes separated with electrolyte. Voltage was applied between the two electrodes. In these simulations, the separation distance of the electrodes was chosen to be 1 μm and the electrodes were simulated as that for Cu. The electrical conductivity of the electrolyte was approximated as 2 S m^{-1}. The COMSOL calculations thus provide a good qualitative insight into the behavior of the working electrode during the CO_2 reduction process.

3. Results and discussion

3.1 Characterization of catalysts

The detailed steps for synthesizing Cu–In inverse opal (CI-1-IO) are shown in Scheme S1 (described in the ESI†). The X-ray diffraction (XRD) patterns of FTO, CI-1, and CI-1-IO are shown in Fig. 1a, which suggest that the hexagonal-phase Cu_2In alloy (JCPDS no. 42-1475, with lattice parameters of $a = b =$

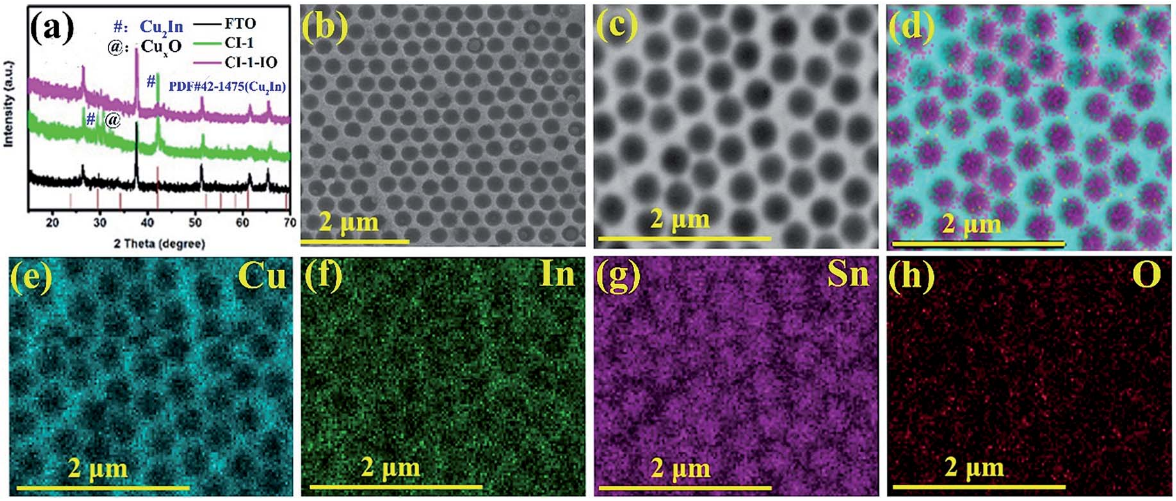

Fig. 1 (a) XRD patterns of FTO glass, CI-1 and CI-1-IO. (b) STEM of CI-1-IO. (c) Selected area for EDS and (d) element mapping of CI-1-IO in the rectangular region shown in (c). (e–h) Separated elemental mapping of Cu, In, Sn and O in the region shown in (d), respectively.

0.4294 nm, $c = 0.5233$ nm) is obtained. Peaks from impurities of Cu_xO can hardly be seen in the XRD pattern of CI-1-IO. The morphology of the CI-1-IO sample is shown in Fig. 1b, which shows a monolayer inverse opal structure (see also Fig. S1†). Fig. 1c and d display the image of an area selected for energy-dispersive spectroscopy analysis and total elemental mapping, respectively. From Fig. 1e–h, it is obvious that the Cu and In elements are distributed on the rim and O and Sn elements from the FTO glass are distributed in the center, which indicates that a monolayer inverse opal structure is formed. The EDX spectra confirm the presence of Cu and In in CI-1 (Fig. S2a†), and Cu, In, Sn and O in CI-1-IO (Fig. S2b†). The morphology and elemental mapping of planar CI-1 were also studied and presented in Fig. S1.† X-ray photoelectron spectroscopy (XPS) analysis shows all three peaks of In^0, Cu^0 and Cu_2O for both CI-1 and CI-1-IO electrodes as shown in Fig. S3.† Interestingly, Sn 3d5 spectra can be detected by XPS on the sample CI-1-IO, while they can hardly be observed on CI-1 suggesting that an inverse opal structure is formed on CI-1-IO. From Fig. 1a and S1,† it can be seen that for CI-1, the surface of the FTO glass is completely covered by the Cu–In nanoparticles. Therefore, no Sn 3d5 peak is observed for the CI-1 sample. The specific analyses of elements are described in Fig. S3.†

The roughness factor (RF) values of the samples were determined from capacitance measurement (details are shown in the ESI†).[51,52] The steady state cyclic voltammetry (CV) curves and the corresponding capacitive scans of FTO, CI-1 and CI-1-IO are displayed in Fig. S4.† The RF of the surface of the substrate (FTO) is taken as 1. The calculated RF of CI-1 and CI-1-IO is about 4.5 and 4.8, respectively. Besides, electrochemical impedance spectroscopy (EIS) was further used to investigate the charge transfer process at the electrode/electrolyte interface. The radius of the CI-1-IO sample is smaller than that of CI-1 (Fig. S5†), which means that the charge transfer resistance of CI-1-IO is smaller than that of CI-1.[53] In turn, it benefits the electron transfer. The Tafel plots of CI-1 and CI-1-IO were studied as well (Fig. S6†). The slopes of both CI-1 and CI-1-IO are greater than 120 mV dec^{-1}, indicating that single-electron transfer is the rate-determining step on both electrodes.[54]

3.2 CO_2 reduction performances of CI-1 and CI-1-IO in a H-cell

CO_2 reduction on CI-1 and CI-1-IO electrodes was performed at different voltages in 0.1 M $KHCO_3$ solution; the results are shown in Fig. 2. It is observed that the $FE_{Formate}$ and FE_{CO} of CI-1-IO are significantly higher than those of the CI-1 catalyst (Fig. 2a and b), indicating that the inverse opal structure might suppress the H_2 evolution reaction (Fig. 2c) and simultaneously facilitate CO_2 conversion. The highest FE of formate formation ($\sim 75 \pm 5\%$) is achieved at -0.6 V *vs.* RHE on CI-1-IO, which is almost 2.7 times higher than that of CI-1 ($\sim 28 \pm 4\%$). Considering that the current density of CI-1-IO is also about 2 times higher than that of CI-I (Fig. 2d), the production rate of formate on CI-1-IO is almost 5.4 times faster than that on CI-1. The CI-1-IO catalyst exhibits much higher electrochemical CO_2 reduction FE than the CI-1 catalyst, especially at low potentials. At -0.6 V *vs.* RHE, the highest FE for CO_2 reduction over CI-1-IO reaches ~92%, which is about 2.6 times higher than that of CI-1 (~36%). Therefore, the inverse opal structure not only increases the CO_2 conversion efficiency but also improves the product selectivity. The improved current density and product selectivity cannot be explained by the exposed FTO surface on the CI-1-IO sample, as our experiments using pure FTO showed very low activity for the CO_2 electrochemical reduction (Fig. S7†). As CI-1 and CI-1-IO possess a similar electrode RF of 4.5 and 4.8, the difference in the surface area of the electrodes cannot be the only reason for the improved activity.

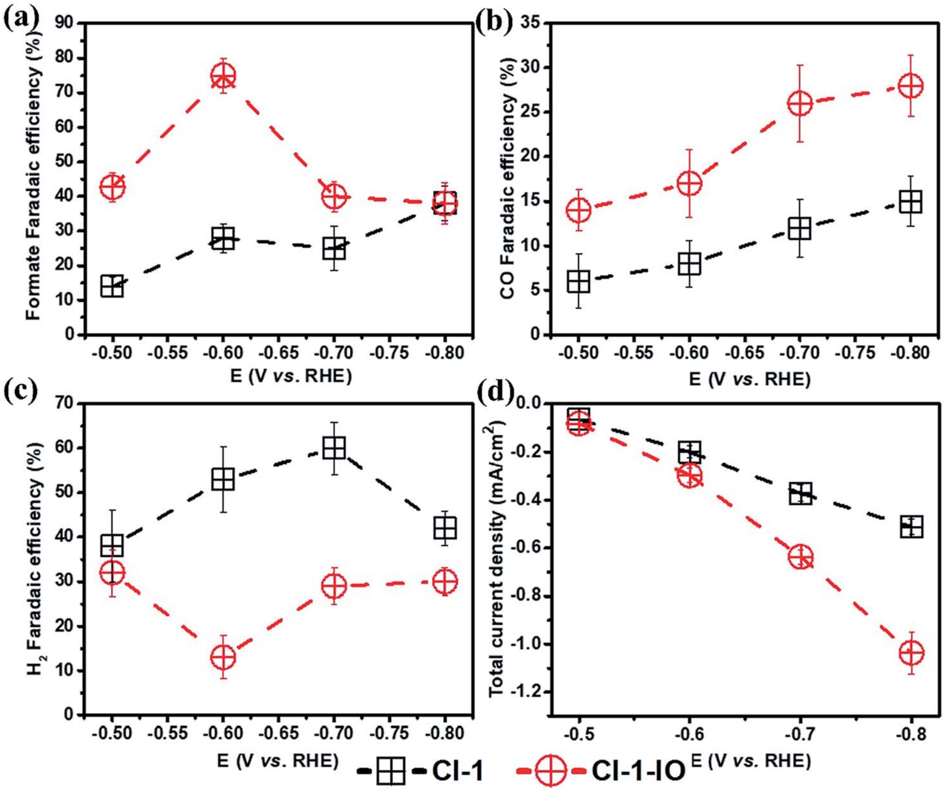

Fig. 2 Faradaic efficiency (FE) of (a) $HCOO^-$, (b) CO and (c) H_2. (d) Total current density over CI-1 and CI-1-IO catalysts in CO_2-saturated 0.1 M $KHCO_3$ solution. The error bar represents the standard deviation of three experiments.

3.3 Mechanism of enhanced CO_2 reduction selectivity and activity

We then further explored the mechanism of enhanced CO_2 reduction selectivity and activity *via* an *in situ* technique and theoretical calculations. Surendranath and coworkers have designed Au and Ag inverse opal thin films with different thicknesses, and the improved CO_2 reduction activity was attributed to the effects of diffusional gradients within the pores of inverse opal.[22,23] However, in this work the inverse opal has a monolayer structure (nanobowl array, no three-dimensional continuous pores), and the effect of diffusion or mass transportation is thus weak. On the one hand, the *in situ* DRIFTS results demonstrate that the Cu–In alloy with an inverse opal structure exhibits faster adsorption kinetics and higher capacity for CO_2 adsorption, as shown in Fig. 3. CO_2 adsorption on the sample surface was studied by introducing a CO_2/H_2O mixture into the reaction cell with a flow rate of 10 mL min^{-1} in the dark. The data were collected every two minutes until the CO_2 adsorption peak was stable (about 28 min). The collected *in situ* DRIFTS spectra are shown in Fig. 3 (see Fig. S8† for more details). The highest peak at about 2364 cm^{-1} can be attributed to CO_2 (gas-phase) adsorption on the sample surface, which shows a fast adsorption equilibrium process (about 2 min) for the gas phase. From Fig. S8a,† we can see that, after 28 min adsorption, the spectral regions of 1000–1800 cm^{-1} and 2688–3500 cm^{-1} for the CI-1-IO surface are obviously higher than that for the CI-1 surface, indicating that CI-1-IO with an inverse opal structure has a higher adsorption ability than CI-1. The broad band at 2688–3500 cm^{-1} corresponds to the increased hydrogen bonding between the CO_2 adsorption products and the hydroxyl groups on the Cu–In alloy surface.[55] The spectral region from 1000 to 1800 cm^{-1} can be assigned to the adsorbed carbonate and bicarbonate, which is shown in detail in Fig. 3c and d (also shown in Fig. S8b and c†), respectively. Specifically, the bands at about 1227 and 1686 may be attributed to the δ_4 (COH) and ν_2 $(OCO)_a$ of vibrational modes of the adsorbed bicarbonate.[55,56] It has been reported that the carbonate bands usually appear at 1200–1700 cm^{-1} and are often observed as broad overlapping bands.[55] The band at about 1566 cm^{-1} may correspond to the bidentate form of adsorbed carbonate, and the peaks at 1057 and 1383 cm^{-1} are associated with the monodentate form of carbonate, usually considered as ν_1 stretching.[55–57] Notably, the intensities of the peaks of carbonate and bicarbonate increase with the increase of CO_2 flow time as shown in Fig. 3c and d, and after 28 min, the intensity of the peaks of CI-1-IO is much stronger than that of CI-1. Specifically, the intensity changes of 1383 and 1227 cm^{-1} are summarized in Fig. 3b. Additionally, the CO_2 adsorption performance on the pre-wetted electrode surface in a closed cell is studied as well (shown in Fig. S9†). It is found that the adsorption of CO_2 (about 2366 cm^{-1}) was saturated for both CI-1 and CI-1-IO in 3 min. Meanwhile, the CI-1-IO sample showed a much higher adsorption capacity for gas-phase CO_2 than CI-1. More details are discussed in the ESI.† The strong adsorption intensity and fast adsorption

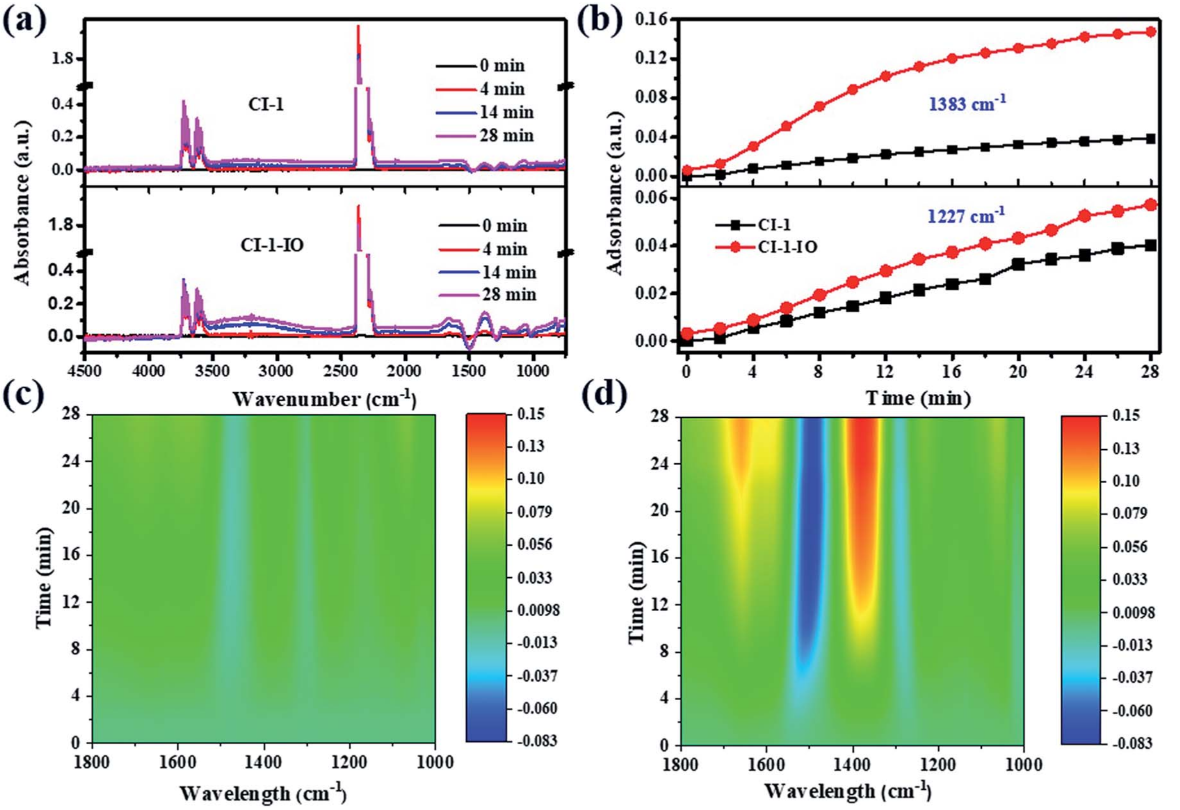

Fig. 3 *In situ* DRIFTS spectra of CO_2/H_2O adsorbed on the CI-1 and CI-1-IO surface. (a) Whole spectra from 750–4500 cm^{-1}, 0 to 28 min. (b) Intensity of specific peaks (1383 and 1227 cm^{-1}) of CI-1 and CI-1-IO. Spectral regions (1000–1800 cm^{-1}) of adsorbed carbonate on the (c) CI-1 and (d) CI-1-IO surface.

equilibrium process demonstrate that CI-1-IO has faster adsorption kinetics and higher capacity for CO_2 adsorption, which would benefit CO_2 conversion.

On the other hand, the high-curvature structures in inverse opal can concentrate the electric field, which affects the ion concentrations near the surface. To understand the mechanism of improved CO_2 reduction on CI-1-IO, we detected the local relative K^+ concentration adsorbed on the electrodes by ion chromatography (IC). The concentration of K^+ adsorbed on the electrode surface was measured using the reported method and the procedure was shown in Fig. S10.†[3] It was found that the K^+ concentration when CI-1-IO was used (50.3 mg L^{-1}) was about 2 times higher than that in the case of CI-1 (24.5 mg L^{-1}).

The influence of K^+ on the CO_2RR was further studied *via* ab initio molecular dynamics simulations. The Gibbs free energy diagrams obtained from density functional theory (DFT) calculations on Cu_2In surface models of different facets at 298.15 K, 1 atom and 0 V *vs.* RHE are shown in Fig. 4. The results indicate that the adsorbed K^+ ions can lower the thermodynamic energy barrier for reaction for all facets. On the Cu_2In (001) facet (Fig. 4a), the adsorbed K^+ ions stabilize the COOH* and HCOOH* intermediates by 1.21 and 1.82 eV, respectively. For Cu_2In (100) and (110) facets, the energy barrier of rate-determining COOH* is lowered by 0.75 and 0.73 eV in the presence of K^+, respectively (Fig. 4b and c). Meanwhile, Fig. 4b and c show that adsorbed K^+ ions stabilize the HCOOH* by 0.48 and 0.6 eV for the Cu_2In (100) and (110) surface, respectively. On the Cu_2In (010) surface (Fig. 4d), the adsorbed K^+ ions lower the energy of COOH* and HCOOH* from 1.09 to 0.48 eV and 0.8 to 0.25, respectively. Simultaneously, the adsorbed K^+ ions also show an ability to lower the thermodynamic energy barrier for the production of CO for all facets (see Fig. S11†) and the optimized structures for different Cu_2In facets with and without K^+ are shown in Fig. S12.† Overall, the results show that the adsorbed K^+ might lower the reaction barrier of COOH*, HCOOH* and CO* intermediates which demonstrates that the adsorbed cations are beneficial for CO_2 reduction.

Based on the results discussed above, it can be suggested that the K^+ ions locally concentrated at the active sites enhance the CO_2RR. The high-curvature structures in an inverse opal can concentrate the electric field, which affects the ion concentration near the surface. Here, a finite-element numerical calculation is employed to study the enhanced field intensification caused by the inverse opal structure. The computed electric field near the sharp edges of the bowl structure is shown in Fig. 4e. The free electron density distribution on the edges of the bowl structure is shown as a color map. The electrostatic field distribution around the edges of the bowl-like structure on the electrode is shown as a group of arrows, where the size and direction of each arrow represent the magnitude and the direction of the electric field. It can be seen that the edges of the bowl structure concentrate electrons. Additionally, a locally

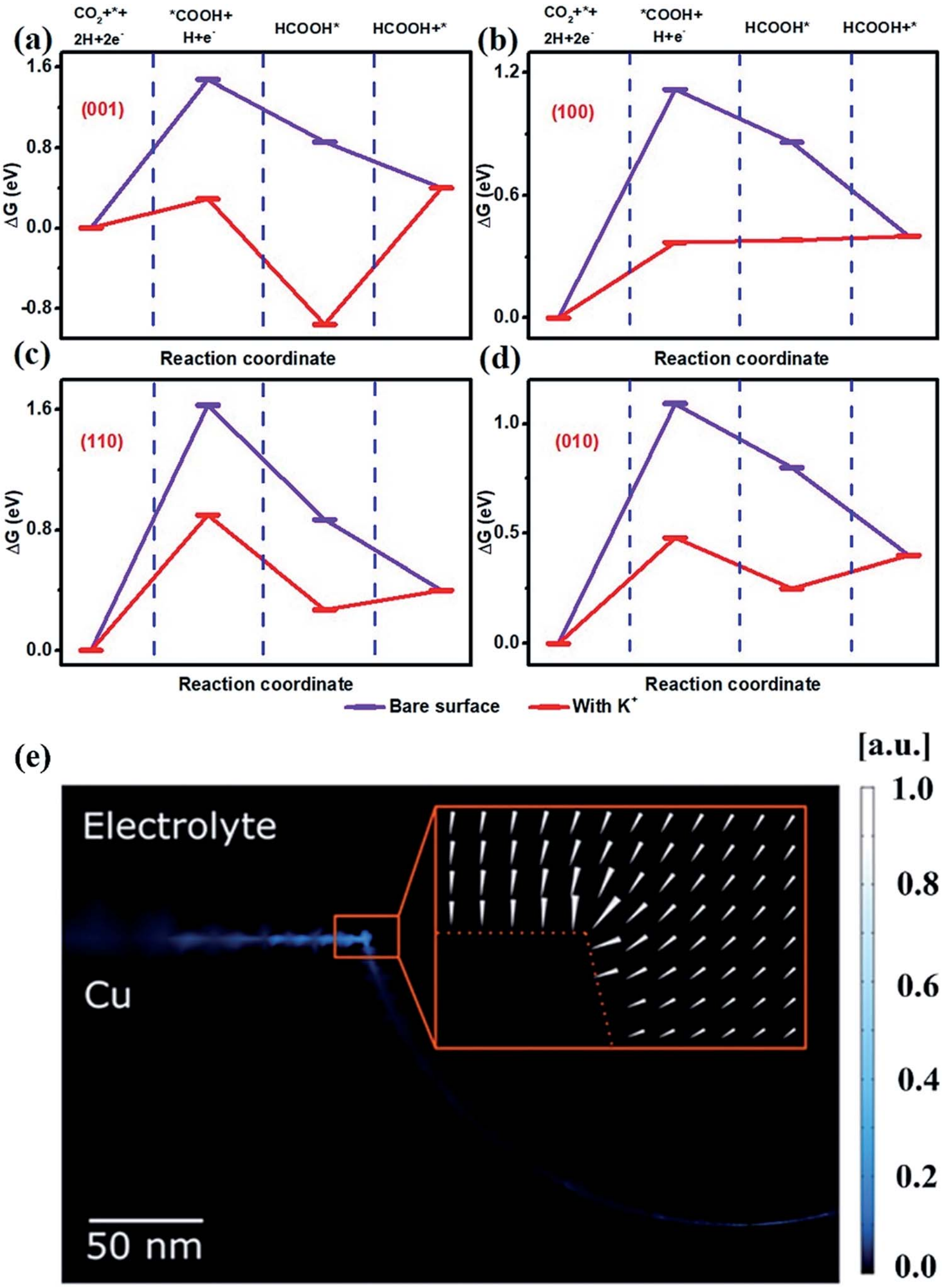

Fig. 4 Thermodynamic barriers for the CO_2 to HCOOH reduction reaction on the Cu_2In surface with and without K^+. Gibbs free energy of electroreduction of CO_2 to HCOOH on Cu_2In (a) (001), (b) (100), (c) (110) and (d) (010) facets in the presence of adsorbed K^+ and without K^+. (e) Computed electron density and the electric field near the surface of the CI-1-IO electrode. The color map presents the normalized free electron density distributed on the surface of the material. The direction and the magnitude of the electrostatic field around the electrode are represented by the white arrows in the inset.

enhanced electrostatic field is generated by the locally concentrated free electron density on the surface of the electrode and points towards the locally concentrated free electron density (arrows in the inset in Fig. 4e). The results can be explained by the migration of free electrons to the regions of the highest curvature on a charged metallic electrode which is a consequence of electrostatic repulsion.

3.4 *In situ* Raman investigation

Raman signals can also benefit from the inverse opal structure, which enhances local electric fields. It is thus of interest to use this structure for *in situ* investigation of the reduction process of CO_2 *via* surface enhanced Raman spectroscopy. Fig. 5a–c show the *in situ* Raman spectra obtained in a tailored cell (shown in Fig. S13†) utilizing an electrolyte containing 7 mL of CO_2 saturated 0.1 M $KHCO_3$ over the CI-1 and CI-1-IO electrodes at

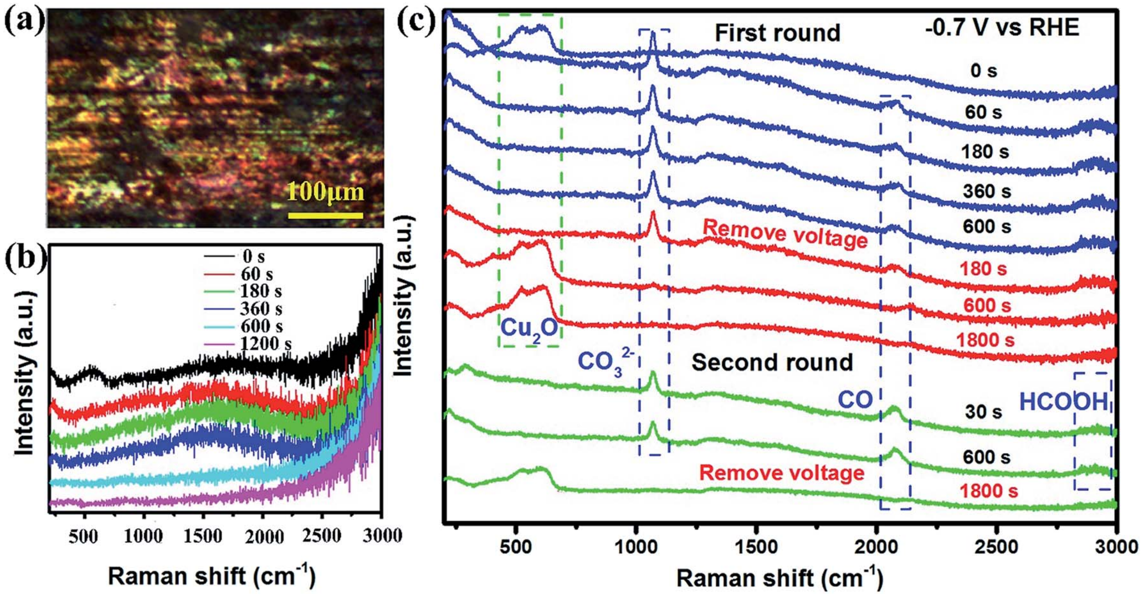

Fig. 5 (a) Microscopy image of CI-1-IO. *In situ* Raman spectra of (b) CI-1 and (c) CI-1-IO during CO_2 reduction at −0.7 V *vs.* RHE in 0.1 M $KHCO_3$.

−0.7 V *vs.* RHE. The chemical composition of the prepared electrodes and their transformations during CO_2 electroreduction were elucidated by Raman spectroscopy (Fig. 5). In the microscopy image of CI-1-IO (Fig. 5a), we can see some bright spots on the electrode surface caused by the inverse opal structure. These are consistent with surface-enhancement of the Raman scattering signal from the chemical compounds on the surface. In Fig. 5b, it can be seen that the Raman signal of the reaction intermediates can hardly be identified on the CI-1 electrode without an inverse opal structure, while the signal is much clearer when the CI-1-IO electrode is used, as shown in Fig. 5c. The Cu–In alloy with an inverse opal structure has a SERS effect, which makes it easier to measure the Raman spectra. Before applying an external voltage (at time = 0 s), the peaks at 219, 526 and 617 cm^{-1} can be assigned to Cu_2O.[23] Within 60 s of applying potential difference, the peaks (at 526 and 617 cm^{-1}) attributed to Cu_2O disappear, which indicates that the catalyst is in the metallic state. Meanwhile, the CO-related peak at 2075 cm^{-1} (CO stretching) appears. A strong signal at 1065 cm^{-1} is also observed, which can be assigned to the stretching mode of the adsorbed carbonate in the interfacial region.[31,35,58] This signal was not observed in recent reports.[16,23,26,33,59] Up to now, how the carbonate forms and whether it affects CO_2 reduction are poorly understood. One view is that carbonate adsorbs on the metal surface through ionic bonds. Such a bond is formed by ligand exchange of HCO_3^- with adsorbed water/hydroxyl followed by deprotonation, which does not participate in the CO_2 reduction reaction.[6,35] Another viewpoint is that the carbonate is formed by activation of CO_2 on the surface oxygen/hydroxyl sites.[6] There is another proposition (proved by the ATR-FTIR spectra) that CO_2 couples with the CO_2^- intermediate first, and is then reduced by another electron resulting in CO and CO_3^{2-} formation.[27] The broad band at about 2900 cm^{-1} can be assigned to the C–H stretching of the formate species.[58,60]

During the study time from 60 to 600 s, the signals of carbonate (1065 cm^{-1}) and CO (2075 cm^{-1}) stretching are steady, indicating that a balance of the reduction reaction is reached. When the voltage is removed for 3 min (the first red curve in Fig. 5c), the intensity of the carbonate and CO stretching signal decreases. The Cu_2O peaks appear again, while the carbonate and CO stretching signals decrease significantly after removing the voltage for 10 min. After removing the voltage for 30 min, the Raman spectrum returns to the original shape before the reaction. Neither the signal from carbonate nor from CO stretching is observed. However, when the voltage is applied again for 30 s, the signal of Cu_2O disappears again, while the carbonate and the CO stretching mode peaks can be observed. After removing the potential for 30 min, the Raman spectrum is similar to that of the first round, indicating the repeatability of the Raman study. These operando Raman spectra demonstrate that the Cu_2O is rapidly reduced to the metallic state upon application of voltage and then the CO_2 reduction reaction occurs on the metal surface. Interestingly, the reduced Cu reoxidizes to Cu_2O after removing the applied voltage. Both the CO_3^{2-} and CO intermediates (CO stretching) can be observed during the CO_2 reduction in the Raman spectra. The inverse opal structure enables more sensitive *in situ* Raman study of the reaction process during the CO_2RR.

To further understand the influence of the inverse opal structure on the electric field at the surface of the electrode, a finite-difference time-domain (FDTD) method was used to calculate the electric field distribution on the Cu–In inverse opal structure when irradiated with light. Fig. 6a and b show the distribution of the electric field (*E*-field) on the surface and the longitudinal profile of the field when the Cu–In monolayer with an inverse opal structure is irradiated with 785 nm light. It can

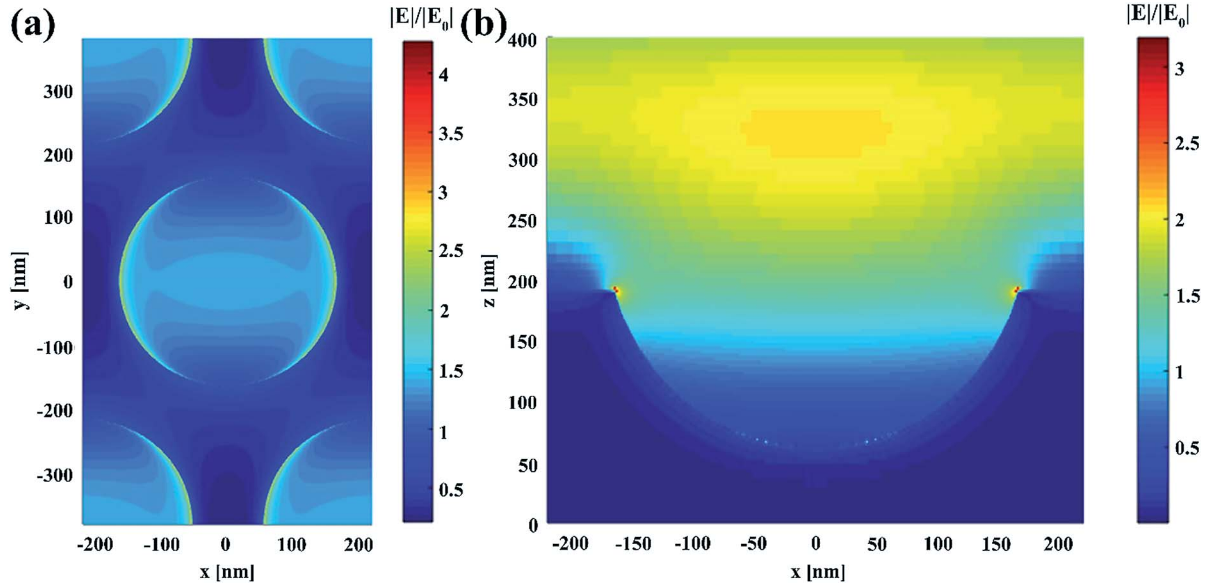

Fig. 6 Electric field distribution simulated for the Cu–In inverse opal structure, when irradiated with 785 nm light, using a finite-difference time-domain (FDTD) method. The direction of light polarization is along *x*. (a) Mapping of the electric field distribution on the surface. (b) Mapping of the longitudinal profile of the electric field distribution.

clearly be seen that the center of the cavity, the top and the sharp edges of the bowl structure show an enhanced *E*-field. Specifically, on the sharp edges of the bowl, the magnitude of the *E*-field is 2–4 times higher. It has been reported that a small increase in the local field can produce large enhancements in Raman scattering (the enhancement scales roughly as E^4).[61] The enhanced Raman signal can also benefit from the improved production rate of CO and formate on CI-1-IO, which is 4.8 and 3.4 times faster than on CI-1 at −0.7 V *vs.* RHE. However, the Raman signal is improved significantly more than this, as seen in Fig. 5b. The Raman signals of the intermediates can hardly be observed on CI-1. Hence, the enhancement of Raman scattering can be mainly attributed to the enhanced electric field on the surface of the inverse opal structure. The "hot edges" present as active sites is also supported by a previous report by Morimoto *et al.*, who used open-loop electric potential microscopy (OL-EPM) to prove that the edge site of porous Zn is the reactive site for CO_2 reduction.[62] Additionally, their OL-EPM results show that the higher current concentration at the edge site is attributed to the increased electric field strength.

4. Conclusions

In summary, we have successfully prepared a Cu–In alloy electrode with an inverse opal structure possessing plenty of "hot edges" for CO_2 reduction and showed that it can be used *in situ* to improve the sensitivity of Raman spectroscopy. The structure not only exhibits higher efficiency for CO_2 reduction, but also dramatically enhances the Raman spectra compared to an Cu–In alloy without an inverse opal structure. DRIFTS results display that the inverse opal structure has faster adsorption kinetics and higher capacity for CO_2 adsorption, which would benefit CO_2 conversion. The Cu–In alloy electrode with an inverse opal structure also concentrates electric fields due to the high curvature structure (COMSOL simulation), and thus concentrates K^+ on the active sites, which lowers the thermodynamic energy barrier of the CO_2 reaction (DFT calculation) and reduces the mean square displacement of CO_2 relative to the surface. The characteristic peaks of the CO intermediates, carbonate and formate were observed on the CI-1-IO electrode. However, these peaks can hardly be observed on the CI-1 electrode. The enhanced Raman signal can be attributed to the inverse opal structure, which enhances the electric field on the sharp edges of the electrode (FDTD simulation). This work introduces the "hot edges" structure as a promising strategy for improving the efficiency and selectivity of the CO_2RR; this structure also enables sensitive *in situ* detection of intermediates *via* SERS and thus provides a way to elucidate the exact mechanism of the electrochemical CO_2RR.

Conflicts of interest

There are no conflicts to declare.

Acknowledgements

The authors gratefully acknowledge financial support from the Ministry of Science and Technology of the People's Republic of China (2016YFE0112200) and National Natural Science Foundation of China (No. 21507011, No. 21677037 and No. 21607027). LO and VKV acknowledge funding and support from the Engineering and Physical Sciences Research Council (EPSRC) Centre for Doctoral Training in Condensed Matter Physics (CDT-CMP), Grant No. EP/L015544/1. VKV acknowledges support from the Royal Society through the University

Research Fellowships and grants CHG\R1\170067, PEF1\170015 and RGF\EA\180228.

References

1 D. Gao, Y. Zhang, Z. Zhou, F. Cai, X. Zhao, W. Huang, Y. Li, J. Zhu, P. Liu and F. Yang, *J. Am. Chem. Soc.*, 2017, **139**, 5652–5655.

2 S. Gao, Y. Lin, X. Jiao, Y. Sun, Q. Luo, W. Zhang, D. Li, J. Yang and Y. Xie, *Nature*, 2016, **529**, 68–71.

3 M. Liu, Y. Pang, B. Zhang, P. De Luna, O. Voznyy, J. Xu, X. Zheng, C. T. Dinh, F. Fan, C. Cao, F. P. de Arquer, T. S. Safaei, A. Mepham, A. Klinkova, E. Kumacheva, T. Filleter, D. Sinton, S. O. Kelley and E. H. Sargent, *Nature*, 2016, **537**, 382–386.

4 Q. Lu, J. Rosen, Y. Zhou, G. S. Hutchings, Y. C. Kimmel, J. G. Chen and F. Jiao, *Nat. Commun.*, 2014, **5**, 3242.

5 J. Qiao, Y. Liu, F. Hong and J. Zhang, *Chem. Soc. Rev.*, 2014, **43**, 631–675.

6 I. V. Chernyshova, P. Somasundaran and S. Ponnurangam, *Proc. Natl. Acad. Sci. U. S. A.*, 2018, **115**, E9261–E9270.

7 J. Rosen, G. S. Hutchings, Q. Lu, S. Rivera, Y. Zhou, D. G. Vlachos and F. Jiao, *ACS Catal.*, 2015, **5**, 4293–4299.

8 H. Kim, H. S. Jeon, M. S. Jee, E. B. Nursanto, J. P. Singh, K. Chae, Y. J. Hwang and B. K. Min, *ChemSusChem*, 2016, **9**, 2097–2102.

9 D. F. Gao, F. Cai, G. X. Wang and X. H. Bao, *Curr. Opin. Green. Sust.*, 2017, **3**, 39–44.

10 H. Zhou, Q. Chen, G. Li, S. Luo, T. B. Song, H. S. Duan, Z. Hong, J. You, Y. Liu and Y. Yang, *Science*, 2014, **345**, 542–546.

11 S. Back, M. S. Yeom and Y. Jung, *ACS Catal.*, 2015, **5**, 5089–5096.

12 G. O. Larrazábal, A. J. Martín, S. Mitchell, R. Hauert and J. Pérez-Ramírez, *ACS Catal.*, 2016, **6**, 6265–6274.

13 A. Jedidi, S. Rasul, D. Masih, L. Cavallo and K. Takanabe, *J. Mater. Chem. A*, 2015, **3**, 19085–19092.

14 Y. Zhou, F. Che, M. Liu, C. Zou, Z. Liang, P. De Luna, H. Yuan, J. Li, Z. Wang, H. Xie, H. Li, P. Chen, E. Bladt, R. Quintero-Bermudez, T.-K. Sham, S. Bals, J. Hofkens, D. Sinton, G. Chen and E. H. Sargent, *Nat. Chem.*, 2018, **10**, 974.

15 C. G. Morales-Guio, E. R. Cave, S. A. Nitopi, J. T. Feaster, L. Wang, K. P. Kuhl, A. Jackson, N. C. Johnson, D. N. Abram, T. Hatsukade, C. Hahn and T. F. Jaramillo, *Nat. Catal.*, 2018, **1**, 764–771.

16 T. T. H. Hoang, S. Verma, S. Ma, T. T. Fister, J. Timoshenko, A. I. Frenkel, P. J. A. Kenis and A. A. Gewirth, *J. Am. Chem. Soc.*, 2018, **140**, 5791–5797.

17 M. B. Ross, C. T. Dinh, Y. Li, D. Kim, P. De Luna, E. H. Sargent and P. Yang, *J. Am. Chem. Soc.*, 2017, **139**, 9359–9363.

18 D. Kim, C. S. Kley, Y. Li and P. Yang, *Proc. Natl. Acad. Sci. U. S. A.*, 2017, **114**, 10560–10565.

19 D. Kim, C. Xie, N. Becknell, Y. Yu, M. Karamad, K. Chan, E. J. Crumlin, J. K. Norskov and P. Yang, *J. Am. Chem. Soc.*, 2017, **139**, 8329–8336.

20 D. Kim, J. Resasco, Y. Yu, A. M. Asiri and P. Yang, *Nat. Commun.*, 2014, **5**, 4948.

21 Z. B. Hoffman, T. S. Gray, K. B. Moraveck, T. B. Gunnoe and G. Zangari, *ACS Catal.*, 2017, **7**, 5381–5390.

22 A. S. Hall, Y. Yoon, A. Wuttig and Y. Surendranath, *J. Am. Chem. Soc.*, 2015, **137**, 14834–14837.

23 Y. Yoon, A. S. Hall and Y. Surendranath, *Angew. Chem., Int. Ed.*, 2016, **55**, 15282–15286.

24 X. Z. Zheng, J. Han, Y. Fu, Y. Deng, Y. Y. Liu, Y. Yang, T. Wang and L. W. Zhang, *Nano Energy*, 2018, **48**, 93–100.

25 D. Ren, Y. L. Deng, A. D. Handoko, C. S. Chen, S. Malkhandi and B. S. Yeo, *ACS Catal.*, 2015, **5**, 2814–2821.

26 M. C. Figueiredo, I. Ledezma-Yanez and M. T. M. Koper, *ACS Catal.*, 2016, **6**, 2382–2392.

27 H. Sheng, M. H. Oh, W. T. Osowiecki, W. Kim, A. P. Alivisatos and H. Frei, *J. Am. Chem. Soc.*, 2018, **140**, 4363–4371.

28 H. Mistry, A. S. Varela, C. S. Bonifacio, I. Zegkinoglou, I. Sinev, Y. W. Choi, K. Kisslinger, E. A. Stach, J. C. Yang, P. Strasser and B. R. Cuenya, *Nat. Commun.*, 2016, **7**, 12123.

29 L. G. A. van de Water, S. K. Wilkinson, R. A. P. Smith and M. J. Watson, *J. Catal.*, 2018, **364**, 57–68.

30 S. Zhu, B. Jiang, W. B. Cai and M. Shao, *J. Am. Chem. Soc.*, 2017, **139**, 15664–15667.

31 G. Kumari, X. Zhang, D. Devasia, J. Heo and P. K. Jain, *ACS Nano*, 2018, **12**, 8330–8340.

32 D. Bohra, I. Ledezma-Yanez, G. Li, W. de Jong, E. Pidko and W. J. A. C. Smith, *Angew. Chem., Int. Ed.*, 2018, **130**, 1–6.

33 D. Ren, J. Fong and B. S. Yeo, *Nat. Commun.*, 2018, **9**, 925.

34 G. Neri, J. J. Walsh, G. Teobaldi, P. M. Donaldson and A. J. Cowan, *Nat. Catal.*, 2018, **1**, 952.

35 L. Mandal, K. R. Yang, M. R. Motapothula, D. Ren, P. Lobaccaro, A. Patra, M. Sherburne, V. S. Batista, B. S. Yeo, J. W. Ager, J. Martin and T. Venkatesan, *ACS Appl. Mater. Interfaces*, 2018, **10**, 8574–8584.

36 Y. Huang, C. W. Ong and B. S. Yeo, *ChemSusChem*, 2018, **11**, 3299–3306.

37 D. Ren, B. S.-H. Ang and B. S. Yeo, *ACS Catal.*, 2016, **6**, 8239–8247.

38 Y. Deng, A. D. Handoko, Y. Du, S. Xi and B. S. Yeo, *ACS Catal.*, 2016, **6**, 2473–2481.

39 Y. Kwon, Y. Lum, E. L. Clark, J. W. Ager and A. T. Bell, *ChemElectroChem*, 2016, **3**, 1012–1019.

40 Z. C. Zeng, S. Hu, S. C. Huang, Y. J. Zhang, W. X. Zhao, J. F. Li, C. Jiang and B. Ren, *Anal. Chem.*, 2016, **88**, 9381–9385.

41 Y. L. Deng and B. S. Yeo, *ACS Catal.*, 2017, **7**, 7873–7889.

42 S. Y. Ding, J. Yi, J. F. Li, B. Ren, D. Y. Wu, R. Panneerselvam and Z. Q. Tian, *Nat. Rev. Mater.*, 2016, **1**, 16021.

43 S. Nie and S. R. Emory, *Science*, 1997, **275**, 1102–1106.

44 X. Z. Zheng, S. G. Meng, J. Chen, J. X. Wang, J. J. Xian, Y. Shao, X. Z. Fu and D. Z. Li, *J. Phys. Chem. C*, 2013, **117**, 21263–21273.

45 J. L. Yuan and C. J. Hao, *Sol. Energy Mater. Sol. Cells*, 2013, **108**, 170–174.

46 P. E. Blochl, *Phys. Rev. B: Condens. Matter Mater. Phys.*, 1994, **50**, 17953–17979.

47 G. Kresse and D. Joubert, *Phys. Rev. B: Condens. Matter Mater. Phys.*, 1999, **59**, 1758–1775.

48 J. P. Perdew, K. Burke and M. Ernzerhof, *Phys. Rev. Lett.*, 1996, **77**, 3865–3868.

49 S. R. Bahn and K. W. Jacobsen, *Comput. Sci. Eng.*, 2002, **4**, 56–66.

50 A. A. Peterson, F. Abild-Pedersen, F. Studt, J. Rossmeisl and J. K. Norskov, *Energy Environ. Sci.*, 2010, **3**, 1311–1315.

51 M. Rahaman, A. Dutta, A. Zanetti and P. Broekmann, *ACS Catal.*, 2017, **7**, 7946–7956.

52 B. Chi, H. Lin and J. Li, *Int. J. Hydrogen Energy*, 2008, **33**, 4763–4768.

53 Y. Yang, F. Teng, Y. D. Kan, L. M. Yang, Z. L. Liu, W. H. Gu, A. Zhang, W. Y. Hao and Y. R. Teng, *Appl. Catal., B*, 2017, **205**, 412–420.

54 S. Rasul, D. H. Anjum, A. Jedidi, Y. Minenkov, L. Cavallo and K. Takanabe, *Angew. Chem., Int. Ed.*, 2015, **127**, 2174–2178.

55 J. Baltrusaitis, J. Schuttlefield, E. Zeitler and V. H. Grassian, *Chem. Eng. J.*, 2011, **170**, 471–481.

56 M. F. Baruch, J. E. Pander, J. L. White and A. B. Bocarsly, *ACS Catal.*, 2015, **5**, 3148–3156.

57 J. Baltrusaitis, J. H. Jensen and V. H. Grassian, *J. Phys. Chem. B*, 2006, **110**, 12005–12016.

58 B. Smith, D. Irish, P. Kedzierzawski and J. Augustynski, *J. Electrochem. Soc.*, 1997, **144**, 4288–4296.

59 J. E. Pander, D. Ren, Y. Huang, N. W. X. Loo, S. H. L. Hong and B. S. Yeo, *ChemElectroChem*, 2018, **5**, 219–237.

60 Y. Ichinohe, T. Wadayama and A. Hatta, *J. Raman Spectrosc.*, 1995, **26**, 335–340.

61 A. Campion and P. Kambhampati, *Chem. Soc. Rev.*, 1998, **27**, 241–250.

62 M. Morimoto, Y. Takatsuji, K. Hirata, T. Fukuma, T. Ohno, T. Sakakura and T. Haruyama, *Electrochim. Acta*, 2018, **290**, 255–261.